Supplement to *Trace metals in soot and $PM_{2.5}$ from heavy-fuel-oil combustion in a marine engine*

J. C. Corbin[1,*], A. A. Mensah[2] S. M. Pieber[1] J. Orasche[3,4] B. Michalke[5] M. Zanatta[1,**] H. Czech[4] D. Massabò[6,7] F. Buatier de Mongeot[6] C. Mennucci[6] I. El Haddad[1] N. K. Kumar[1] B. Stengel[8], 9 Y. Huang[4] R. Zimmermann[3,4,9] A. S. H. Prévôt[1] M. Gysel[1]

[1]Laboratory of Atmospheric Chemistry, Paul Scherrer Institute, CH-5232 Villigen, Switzerland

∗Now at: Measurement Science and Standards, National Research Council Canada, 1200 Montreal Road, Ottawa, K1A 0R6, Canada

[2]Institute for Atmospheric Chemistry, ETH Zurich, 8092 Zurich, Switzerland

[3]Joint Mass Spectrometry Centre, Cooperation Group Comprehensive Molecular Analytics, Helmholtz Zentrum München, Ingoldstädter Landstr. 1, 85764 Neuherberg, Germany [4]Joint Mass Spectrometry Centre, Chair of Analytical Chemistry, Institute of Chemistry, University of Rostock, Dr.-Lorenz-Weg 2, 18059 Rostock, Germany

[5]Research Unit Analytical Biogeochemistry, Helmholtz Zentrum München, 85764 Neuherberg, Germany

∗∗Now at: Alfred Wegener Institute, Am Handelshafen 12, 27570 Bremerhaven, Germany

[6]Department of Physics, University of Genoa, Via Dodecaneso 33, 16146 Genova, Italy [7]INFN, Sezione di Genova, Via Dodecaneso 22, 16146 Genova, Italy

[8]Department of Piston Machines and Internal Combustion Engines, University of Rostock, Albert-Einstein-Strasse 2, 18059 Rostock, Germany [9]HICE – Helmholtz Virtual Institute of Complex Molecular Systems in Environmental Health, Germany

Correspondence to: Martin Gysel (martin.gysel@psi.ch)

Additional ICP-OES method details

Elements were analyzed using the ICP-OES system "Spectro Ciros Vision" from SPECTRO Analytical Instruments GmbH & Co. KG, Kleve, Germany. Samples were introduced to the instrument using its peristaltic pump, followed by nebulization with a Seaspray nebulizer utilizing a cyclone spray chamber. The nebulizer flow rate was $0.6\,\mathrm{L\,min^{-1}}$, the plasma gas flow rate was $14\,\mathrm{L\,Ar\ min^{-1}}$, and the RF power was set to 1200 W. For diesel fuel (EN 590), we followed the analysis standard DIN EN 16476 for direct determination of Na, K, Ca, P, Cu, Zn in diesel fuels by ICP-OES. For HFO we followed the ICP-OES standards DIN 51400-10 for determination of sulfur; ISO 10478 for determination of Al and Si; and DIN EN 15944 for determination of Ni and V. These standards also apply to other elements.

The measured elements and spectral element lines were Al (167.078 nm), As (189.042 nm), Ba (455.404 nm), Ca (183.801nm), Cd (214.438 nm), Co (228.616 nm), Cr (267.716 nm), Cu (324.754 nm), Fe (259.941 nm), K (766.491 nm), Mg (279.079 nm), Mn (257.611 nm), Mo (202.030 nm), Na (589.592 nm), Ni (231.604 nm), P (177.496 nm), Pb (220.353 nm), S (180.731 nm), Sb (206.833 nm), Se (196.090 nm), Sn (189.991 nm), Sr (407.771 nm), Ti (334.941 nm), V (292.464 nm), Zn (213.856 nm).

After every ten measurements, three blanks and a control (certified standard) were measured for all mentioned elements. Results were calculated using a computerized lab-data management system, relating the sample measurements to calibration curves, blank determinations, control standards and the weight of the digested sample. The determination method was validated by regular laboratory intercomparison studies and by regular analysis of adequate certified reference materials.

The digestion procedure and solubilisation of metals from filter samples and subsequent element determination were evaluated with certified reference material (CRM) "BCR 723 road dust, additional values". This CRM was considered as comparable to samples from this study, as it is collected from ceiling of a tunnel being a main route for inter-Europe diesel trucks. The recoveries ranged mainly between 80–109%.

Detailed recoveries per element are given in Table S4. The recovery of Ni in the CRM was an outlier at 65.5 %, is consistent with our previous experience for Ni oxides. The expected recovery for Ni in other compounds, such as organometallic compounds, is closer to 90–100 % in our experience. Therefore, to the extent that our HFO samples contained Ni in oxide form, our reported values may be biased low (such that V : Ni is biased high). The excellent agreement between our reported values with the literature (see main text) suggests that such potential issues are not prominent in our data set. However, as previous work has not reported Ni recoveries in detail, we cannot exclude the possibility that literature values are also biased low due to the presence of Ni in its oxide form.

Additional discussion of AMS analysis and results

AMS bounce related correction

Because solid nrPM may bounce off of the porous-tungsten vaporizer, a bounce-related correction factor known as the collection efficiency (CE_b) is routinely applied to AMS data[1]. In this study, OM was likely liquid since a large fraction[2], though not all[3,4], of its mass originated from lubrication oil. Similarly, sulfates were likely liquid sulfuric acid because negligible concentrations of ammonium or nitrate were measured. Therefore we have applied a bounce-related collection efficiency of unity, reflecting no correction for bounce[5].

Elemental analysis and OM/OC ratios

Aiken et al.[6] showed that electron-ionization mass spectra can be calibrated for O:C and H:C ratios (from which OM/OC can be derived when OM is known). In normal AMS operation, H_2O-related ions and CO_2^+ suffer from interference from background water and carbon dioxide, respectively. Other complications arise due to the thermal

degradation reactions on the AMS porous-tungsten vaporizer, for example dehydration reactions. Aiken et al.[7] proposed an empirical model to address these complications in normal AMS operation. Canagaratna et al.[8] showed that some biases that resulted from the Aiken et al.[7] could be improved by increasing the complexity of the empirical model.

In this study, we have chosen to use the Aiken et al.[7] elemental analysis method rather than the new Canagaratna et al.[8] method. The extensions to the empirical model proposed by Canagaratna et al.[8] are relevant to reactions such as dehydration, which cannot occur in the almost oxygen-free OM that was measured in this study. Thus, the quantification of the additional parameters required for the more-complex Canagaratna model would only enhance our uncertainty in the reported elemental composition.

Additional discussion of SP-AMS analysis and results

Methodology for SP-AMS metal quantification

Our quantification of metals by SP-AMS can be summarized is generally based on the application of the method described by Carbone et al. (2015). We carefully considered each assumption involved in applying this method, and discuss the method and our considerations in this supplementary section.

The RIE (sensitivity relative to nitrate in ammonium nitrate, as defined in the main text) used for SP-AMS-measured rBC was 0.2[9], a value which includes the transmission efficiency of rBC particles from the aerodynamic lens to the SP-AMS laser (E_z) as discussed further below. For SP-AMS metals, we used the RIEs reported by Carbone et al.[10]: 1.36 (V), 0.25 (Ni), 0.32 (Fe), 21.42 (Ba), and 20.30 (Na). The RIEs reported by Carbone et al.[10] for Na and Ba are anomalously high due to thermal surface ionization (TSI). Since Carbone et al.[10] determined these RIEs by vaporizing monolayers of

metal nitrates on rBC particles, most of the metal mass in their study would have been subject to TSI. In contrast, if metals existed as heterogeneous inclusions in our rBC particles (soot), some of the metal mass may have vaporized from a metal or metal-oxide surface. This may have suppressed TSI, for which the work function of the surface is an essential parameter[11,12]. Since TSI enhances the RIE, and since $C_{\mathrm{M,SP\text{-}AMS}}$ decreases with increasing RIE, our reported values for $C_{\mathrm{Ba,SP\text{-}AMS}}$ and $C_{\mathrm{Na,SP\text{-}AMS}}$ are conservative lower limits. The relevance of TSI is dependent on the mass fraction of Na or Ba vapourized from low-work-function surfaces in the SP-AMS. It is unlikely that this factor is large enough to bias the conclusions made in this manuscript because previous work has not observed the presence of Na or Ba inclusions in HFO soot[13,14]. To minimize the impact of TSI on this manuscript, we have limited our interpretation of Na and Ba to the emission factors presented in the manuscript. As just stated, the possibility of TSI means that these are conservative concentration estimates.

We note that there is a possibility that some fraction of our measured SP-AMS signals have have originated from metals or metal oxides which directly absorb the 1064 nm laser. The good correlation between $C_{\mathrm{rBC,SP\text{-}AMS}}$ and $C_{\mathrm{M,SP\text{-}AMS}}$ for all samples but the Fe outlier in Fig. 2 of the manuscript indicates that this fraction was minor except for that outlier. This good correlation stands in contrast to the very poor correlation between $C_{\mathrm{M,SP\text{-}AMS}}$ and $C_{\mathrm{M,ICP\text{-}OES}}$ shown in Figure S9.

Each SP-AMS metal concentration was quantified from its most-abundant isotope-ion signal. These isotopic signals were integrated to obtain peak areas which were then divided by the relative abundance[15] of that isotope. The mass fraction of Fe (12 %) and V (3.5 %) present as metal-oxide ions (MO_x^+) was added to the corresponding mass of metal ions (M_x^+) when reporting the mass concentrations of these species.

We estimated peak-specific limits of quantification (i.e., method limits of quantification, LOQ) to be similar for all quantified metals, as 20 ng m^{-3} by the following novel procedure. The procedure is based on inspection of the measured isotopic abundances as a function of the measured concentrations. At lower concentrations, the variance of the measured abundances increased rapidly due to the imprecise measurement of

the less-abundant isotope. We define the LOQ to have been reached just before this rapid increase (at roughly $> 30\,\%$ imprecision), as is clearly visible in the scatterplots in Figs. S5–S7. We thus obtained an estimated LOQ of $20\,\mathrm{ng\,m^{-3}}$ for all quantified metals except Ni, for which the estimated LOQ was $5\,\mathrm{ng\,m^{-3}}$. This approach actually evaluates the precision with which the less-abundant isotope was quantified, although the more-abundant isotope was used to calculate mass concentrations (Methods section of manuscript). Correspondingly, this approach results in a conservative estimate of the LOQ. The estimated LOQ is in reasonable agreement with the uncertainties provided from SP-AMS peak-fitting errors[16] (error bars in Figs. S5–S7). Note that we did not use the standard definition of LOQ (10 times the standard deviation of a blank) because of the potential importance of interference from nearby peaks in our method of quantification.

SP-AMS particle-size sensitivity

Particles are introduced into the SP-AMS by an aerodynamic lens[17] which focusses particles into a narrow beam. When this particle beam arrives at the vaporizers, it has a cross section such that nearly all particles with diameters d_{va} (the free-molecular aerodynamic diameter) between about $90-600\,\mathrm{nm}$ impact the porous-tungsten vaporizer. That is, the transmission efficiency from lens to porous-tungsten vaporizer (E_L) is near unity. The corresponding transmission efficiency from lens to laser vaporizer (E_z) is smaller than E_L, since the laser has a smaller cross section[18,19].

The amount by which $\mathrm{E}_z < \mathrm{E}_L$ will depend on the particle d_{va}. This dependence is counter-intuitive due to the following relationship of d_{va} with soot-particle mixing state. For fractal-like soot particles, d_{va} is independent of the particle mass to a good approximation, because it is primarily governed by the soot-monomer diameter[20]. For spherical particles d_{va} is the volume-equivalent diameter weighted by the overall particle density[21]. Therefore, a difference in E_z between two experiments may indicate either a difference in soot-monomer diameters, a difference in the fraction of nrPM mixed with the soot, or both.

Note that, in the absence of internally-mixed nrPM, the dependence of d_{va} on soot-monomer diameter means that $E_z < 1$ does not bias the measurements towards larger particles. In this scenario, normalizing SP-AMS metal signals to rBC signals provides an estimate of the metal content of the rBC that is not biased by d_{va}.

Evaluation of SP-AMS response to rBC

SP-AMS rBC quantification

As stated in the main text, SP-AMS rBC mass concentrations $C_{\mathrm{rBC,SP\text{-}AMS}}$ were quantified from the sum of carbon-cluster ions ($C_{1\text{-}9}^{+}$)[9,22,23]. Fig. S1 shows that the ratio $C_1^{+} : C_3^{+}$ was unity for our samples, in contrast to the previously-reported[22] of 0.6. Note that this ratio was independent of fuel type in our study, in contrast to the results of Corbin et al.,[22] who found that a quenched propane flame could produce different ratios depending on the global equivalence ratio of the flame.

In addition major carbon cluster ions, fullerene-related carbon-cluster ions, such as C_{32}^{+} were also observed, but at negligible ($\ll 1\,\%$ of $C_{1\text{-}9}^{+}$) concentrations. Signals from oxidized rBC-surface functional groups[24] were also identified, but were too low to be quantified, partly due to high OM concentrations.

Comparison of SP-AMS rBC with SP2 rBC

rBC concentrations estimated by SP-AMS were not correlated with BC measurements from two independent methods: rBC by SP2 and absorption by in-situ extinction-minus-scattering (Fig. S3). These measurements are described in detail elsewhere[25]. This section describes this lack of correlation in detail.

The ratio $C_{\mathrm{rBC,\ SP\text{-}AMS}} : C_{\mathrm{rBC,\ SP2}}$ in Fig. S3 was close to unity for the fuels MGO and diesel, and for low C_{OM}. This result supports that the SP-AMS behaved as expected, since the SP-AMS RIE used here was been obtained for irregularly shaped BC particles[9], which have a lower E_z than BC mixed with OM[18]. Note that due to the fact that d_{va} for fractal-like aggregates is governed by soot-monomer size rather than

soot-particle mass[20], the SP-AMS RIE calibration is not independent of E_z when using realistic, fractal-like soot particles; differences in soot-monomer size between calibrant and sample will therefore lead to biases such as we have observed. Such differences are indeed expected a priori; the monomer size of HFO soot has been reported as 30–80 nm[14,26] whereas that of the calibrant material (the fullerene-rich carbon black known as Fullerene Soot; FS) is $\sim$ 50 nm[27]. Moreover, FS is not fractal-like[27].

The difference in monomer size and morphology of the FS calibrant compared to the real soot samples means that the SP-AMS E_z (the instrument transmission efficiency from aerodynamic lens to laser vaporizer; see Experimental Section) must be different for the sampled particles compared to the calibration particles. If the monomer size of the sampled particles varied over time, then the SP-AMS sensitivity (E_z) would vary as well. Such wide variation is shown in Fig. S3, where the ratio $C_{\mathrm{rBC,\ SP\text{-}AMS}} : C_{\mathrm{rBC,\ SP2}}$ is plotted against $C_{\mathrm{rBC,\ SP2}}$ in Fig. S3. The figure includes HFO (the main focus of this manuscript) as well as the distillate fuels MGO and diesel for context. Colours indicate the AMS-measured OM concentration C_{OM}. In addition to monomer size and morphology effects, mixing state effects[18,19] may be present in the figure, however as mentioned we believe internal mixing of the rBC to be negligible.

The ideal value of $C_{\mathrm{rBC,\ SP\text{-}AMS}} : C_{\mathrm{rBC,\ SP2}}$ (the ordinate axis in Fig. S3) is unity, since the SP2 provides a reliable, mixing-state-independent measure of rBC mass concentrations[28,29], This value would reflect a perfectly-calibrated SP-AMS. That is the best-case scenario; the second-best case scenario is for this ratio to be a constant number, reflecting a constant SP-AMS sensitivity; for example if the collection efficiency was incorrect. While the ratio approached unity for some samples (corresponding to an accurate RIE of rBC) no constant ratio was evident for any sample.

We are confident that biases in $C_{\mathrm{rBC,\ SP2}}$ due to particle-sizing limitations do not play a role in the trends of Fig. S3 because the slope of a plot of the 780 nm absorption coefficient (measured simultaneously by the extinction-minus-scattering technique) with $C_{\mathrm{rBC,\ SP2}}$ was near constant, at 7.8 $\mathrm{m^2 g^{-1}}$ (the standard error of the fit was $\pm$ 23 %). This ratio is equal to the BC mass absorption cross-section. Those ab-

sorption measurements, presented in Corbin et al.[25], were performed on the aerosol ensemble and were not subject to single-particle limitations. Also, the extinction-minus-scattering instrument was located physically next to the SP2 and SP-AMS, such that any particle losses in the sampling lines would be similar between these three instruments.

While Fig. S3 shows some dependence of this ratio on both fuel type and C_{OM} (potentially indicating internal mixing), the scatter for any given fuel is too large to recommend constant-valued fuel-specific calibration factors. In particular, the scatter is very large for HFO, for which rBC-containing particles were very large[25]. In these experiments, approximately half of the rBC mass for HFO was found in particles with spherical-equivalent diameters d_e larger than 700 nm[25], which corresponds to free-molecular-regime aerodynamic diameters $d_{va} = \hat{\rho_p} d_e / \chi$ of $420 - 630$ nm, assuming a specific gravity $\rho_p = 1.8$ and shape factor $\chi = 2 - 3$, based respectively on Park et al.[30] and Sorensen[31]. A more-accurate calculation of d_{va} is not possible due to the uncertainty in estimating χ.) This is the size range within which AMS lens transmission efficiency begins to fall below unity[17]. The SP2-measured size distribution was similar for all HFO experiments[25] and the SP-AMS and SP2 sampled adjacently to one another, so our confidence in the SP2 correction factor (see Experimental section of manuscript) is much higher than our confidence in the SP-AMS lens transmission. Thus, we believe that variations in BC-particle size are the main cause of the variable ratio in Fig. S3.

It could be hypothesized that an interference of OM ions could explain the variable ratios in Fig. S3. However, the correlation of C_3^+ (the major SP-AMS ion from BC, Corbin et al.[22]) with its nearest neighbour, $H_2\,{}^{34}S^+$, was less than 0.02. In contrast, the correlation of C_3^+ with C_1^+ was very good (Fig. S1, slope of unity) and the correlation of C_3^+ with the sum C_{1-5}^+ was better than 0.99 (Pearson r^2). The latter correlation also illustrates that organic-generated C_1^+ was negligible in this study, in contrast to the conclusions of Corbin et al.[22]. Organic-generated C_3^+ was also negligible, in agreement with literature[19,22]. Here, we do not intend to imply that internal mixing

of OM and rBC was significant, only that the ions generated from these two species may overlap in the mass spectrometer. If internal mixing was significant, it is expected to increase E_z Willis et al.[18], Ahern et al.[19], but as already stated Corbin et al.[25] concluded that internal mixing was minor for this data set.

It could also be hypothesized that variations in the SP-AMS ionization efficiency of rBC ions contributed to the variable ratios in Fig. S3. We believe that this is unlikely, since the 780 nm mass-absorption cross-section of these samples was stable for all experiments[25], however, stronger evidence would be needed to address this hypothesis.

In addition to the small-x ($x < 10$) C_x ions discussed above, larger fullerenic clusters were observed in small relative amounts in this study (less than 1 %). However, the quantification of these clusters was not considered reliable due to the abundance of high-m/z signals from organic ions in the mass spectrum, so they are not discussed further.

Metal ions observed by SP-AMS

With the 1064 nm SP-AMS laser switched on, metal ions appeared in the mass spectrum (see Fig. S2 for an example) as well as carbon-cluster ions. This subsection discusses the metallic ions; the carbon-cluster ions were discussed in the preceding section.

The three most-abundant metals present in HFO were V, Ni, and Fe. The negative mass defects of these ions helped to separate them from nearby organic peaks, allowing reliable identification and quantification. These metals were resolved in the SP-AMS mass spectrum as atomic ions (M^+). Cluster ions (M_n^+) were not observed, potentially because the M^+ ions were formed from ionization of M(g), although fragmentation of larger gas-phase molecules cannot be ruled out.

In addition to these major species, Na, K, and Ba were measured with excellent signal-to-noise due to surface-ionization-enhanced SP-AMS sensitivity[10], as was discussed above. K is noted here but was not quantified because its SP-AMS ionization efficiency has not been reported. The measured isotopic ratios for Ni (Fig. S6), Fe

(Fig. S7), and Ba (Fig. S8) were in excellent agreement with the literature[15].

Some less-abundant metals which were measured in the $PM_{2.5}$ by ICP-OES (e.g., Zn^+, Cu^+, and Mo^+) could be identified in selected mass spectra, but were not of sufficient intensity to be quantified[16,32] in most spectra due to the frequent presence of overlapping, more-intense organic-ion peaks. Nevertheless, the quantified metals include the five most-abundant $PM_{2.5}$ trace elements except calcium (see Fig. 1 and Table S3). Calcium could not be quantified as calcium-40 suffered interference from argon and calcium-42 suffered interference from organic ions. Similarly, aluminum (the sixth most-abundant metal) suffered interference from nitrogen-28. Silicon (which, though not a metal, was the tenth most-abundant element in the fuel) was not observed in atomic nor molecular ions.

In addition to monoatomic metal ions (M^+), some metal-oxide ions (MO^+) ions were observed, always in minor quantities. Specifically, the ions FeO^+, Fe_2O^+, and VO^+ were observed, at much lower intensities than the respective metal-only ion signals (see scatterplots in Figs. S5 – S8). In particular, 3.5 % of the total measured V mass was present as the oxide ion (Table S5), showing that the majority of V was ionized from V(g), since the species VO^+ is stable enough to survive the high ionization energies used in laser desorption/ionization mass spectrometers[33–36] and would therefore have survived electron ionization in the SP-AMS. This V(g) may have vapourized directly from metallic compounds or have been formed by the thermal decomposition of metal oxides[37]. In contrast to V, the mass of Fe observed as FeO^+ was relatively high at 12 % (Table S5), suggesting that iron oxide vapours were formed prior to electron ionization.

Other metal-oxide ions (such as $FeO_2{}^+$, NiO^+, Ni_2O^+, $VO_2{}^+$, and BaO^+) were not observed. When reporting metal mass concentrations, we have reported the total measured mass of each metal, which means including the small fraction of M present as $M_xO_y^+$ in the reported metal mass concentrations. After correcting for the presence of oxygen in the oxides, this corresponds to an increase in the reported concentrations by 12 % (Fe) and 3.5 % (V), as shown in Table S5.

Table S1: Abbreviations and symbols commonly used in the text.

Abbreviation	Definition
HFO	Heavy Fuel Oil (residual fuel)
MGO	Marine Gas Oil (distillate fuel)
DF	Diesel Fuel (distillate fuel)
BC	Black Carbon (strongly light-absorbing, refractory to 4000 K, insoluble graphenic formed by incomplete combustion)
rBC	refractory Black Carbon, defined when BC is quantified by SP2 and also used for the SP-AMS.
SP2	Single Particle Soot Photometer
SP-AMS	Soot-Particle Aerosol Mass Spectrometer
AMS	Aerosol Mass Spectrometer (or dual-vaporizer SP-AMS operating with laser off)
ICP-OES	Inductively-Coupled-Plasma Optical Emission Spectroscopy
OM	Condensed organic matter (organic PM)
PM	Particulate Matter
SEM	Standard error of the mean
soot	Particle composed primarily of aggregated BC monomers, produced by in-flame nucleation and coagulation, including inclusions and internally-mixed components.
char	Particle composed primarily of large, spherical BC, produced by fuel-droplet pyrolysis.
C_x	Mass concentration of x
d_{va}	Free-molecular regime aerodynamic diameter

Table S2: Elemental composition of the fuels , obtained by ICP-OES. Selected physical properties are also shown. All percentages and ppm are by mass.

Parameter	Unit	Residual fuel (HFO)	Diesel (DF)	Marine gas oil (MGO)
Fuel density[a]	$\mathrm{kg\,m^{-3}}$	989.5	833.8	833.9
Viscosity[b]	$\mathrm{mm^2\,s^{-1}}$	341.9	2.68	2.83
Heating value	$\mathrm{kJ\,kg^{-1}}$	39871	42708	42675
C	%	85.91	85.3	85.12
H	%	11.23	13.91	13.89
O	%	0.56	< 0.01	< 0.01
S	ppm	23306	7.0	783
Ash[c]	%	0.03	< 0.01	< 0.01
V	ppm	138	< 0.1	< 0.1
Ni		31.3	< 0.1	< 0.1
Na		29.2	< 0.1	< 0.1
Ca		24.8	< 0.1	< 0.1
Fe		14.3	< 0.1	0.2
Si		2.6	< 0.1	< 0.1
Al		1.6	< 0.1	< 0.1
Zn		1.4	< 0.1	< 0.1
P		1.3	< 0.1	< 0.1
Cr		1.0	< 0.1	< 0.1
K		0.7	< 0.1	< 0.1
Cu		0.7	< 0.1	< 0.1
Ba		0.6	< 0.1	< 0.1
Mo		0.5	< 0.1	< 0.1
Mn		0.5	< 0.1	< 0.1
Mg		< 0.1	< 0.1	< 0.1
Pb		< 0.1	< 0.1	< 0.1
Sn		< 0.1	< 0.1	< 0.1

[a]Measured at 288 K. [b]Measured at 323 K for HFO, at 313 K otherwise.

Table S3: Elemental composition of the residual fuel and residual-fuel $PM_{2.5}$ (after engine combustion and filter sampling), obtained by ICP-OES.

Element	Residual-fuel sample [$mg\,kg^{-1}$ fuel]	Residual-fuel $PM_{2.5}$ [$mg\,kg^{-3}$ fuel]
V	138	17.05 ± 0.38
Ni	31.3	3.22 ± 0.10
Na	29.2	3.71 ± 0.13
Ca	24.8	3.16 ± 0.21
Fe	14.3	2.46 ± 0.16
Si	2.6	n.d.
Al	1.6	1.52 ± 0.25
Zn	1.4	0.66 ± 0.05
P	1.3	0.50 ± 0.06
Cr	1.0	0.11 ± 0.01
Cu	0.7	0.15 ± 0.01
K	0.7	0.45 ± 0.08
Ba	0.6	0.176 ± 0.006
Mo	0.5	0.056 ± 0.002
Mg	< 0.1	0.31 ± 0.06
Mn	0.5	0.033 ± 0.003
Pb	< 0.1	< 0.0015
Sn	< 0.1	0.074 ± 0.005
Total	110.5	33.66

n.d.: not determined.

Table S4: ICP-OES recoveries of Certified Reference Material "BCR 723 road dust, additional values". n.r.v.a. = no reference value available.

Element	Recovery
Al	95.3%
As	91.6%
B	n.r.v.a.
Ba	92.8%
Be	n.r.v.a.
Ca	96.2%
Cd	83.2%
Co	80.2%
Cr	80.9%
Cu	90.5%
Fe	109%
Hg	n.r.v.a.
K	107%
Li	n.r.v.a.
Mg	100%
Mn	91.7%
Mo	80.0%
Na	101%
Ni	65.5%
P	n.r.v.a.
Pb	92.3%
S	84.6%
Sb	78.0%
Sn	99.1%
Sr	90.6%
Ti	104.7%
V	92.7%
Zn	85.9%

Table S5: SP-AMS-measured mass fraction of oxides relative to atomic ions, for species with detectable oxide signals. The concentration ratios are obtained from the fits in Figs. S6 and S7. The quantity $C_{\text{M-in-oxide-ion}}$ is the mass concentration of M present in that oxide ion.

Metal M	Oxide ion	$C_{\text{oxide-ion}} : C_{\text{M}}$ [%]	$C_{\text{M-in-oxide-ion}} : C_{\text{M}}$ [%]
V	VO^+	4.64 ± 0.08	3.53 ± 0.06
Fe	FeO^+	12.8 ± 0.7	9.95 ± 0.5
Fe	Fe_2O^+	5.1 ± 0.4	2.23 ± 0.15
Fe	*total*	17.9	12.18

It has been assumed that metal oxides have similar RIEs to the metal ions themselves. The conclusions made in this manuscript are insensitive to the metal-oxide RIE.

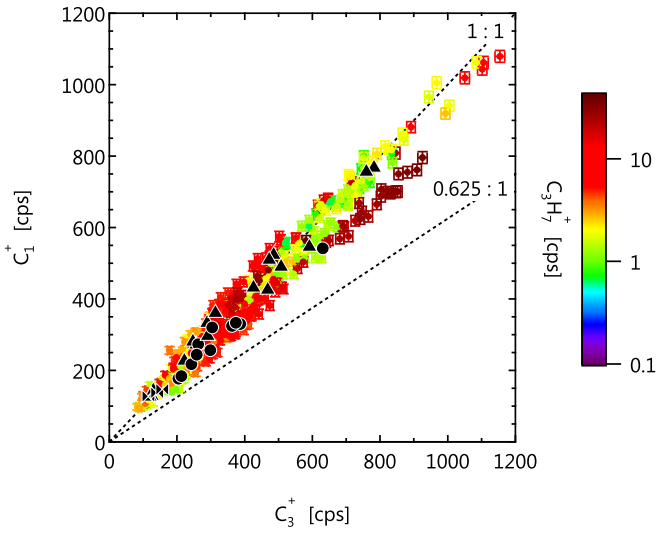

Figure S1: Relationship between C_1^+ and C_3^+. Colours indicate the signal at $C_3H_7^+$, as indicator of OM concentration. Small symbols indicate individual measurements. Large black symbols indicate filter-sample averages, and are coded for HFO (●) or the two distillate fuels MGO (■) and diesel (▲). Data outside of filter-sampling periods are not shown in this figure. The high-OM points slightly below the 1 : 1 line are also the HFO points, so the cause of their deviation is unclear. Slope of 0.625 is that measured by Onasch et al.[9], which is used as the default software value; we applied 1.0 instead.

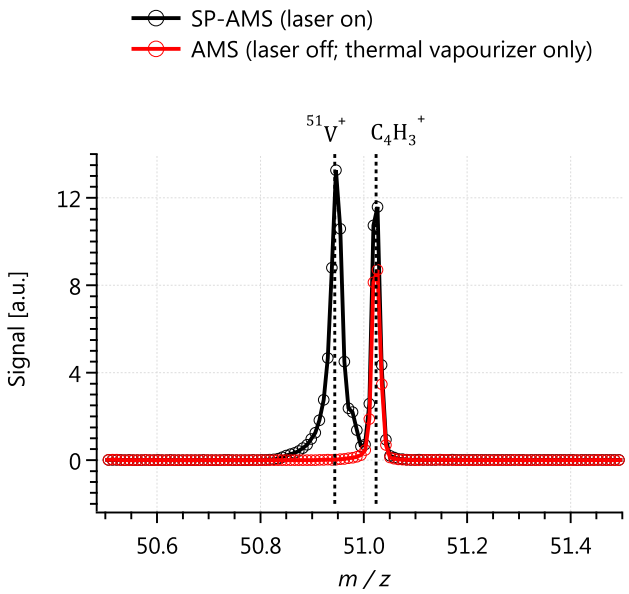

Figure S2: Mass spectrum at m/z 51 with 1064 nm laser on (SP-AMS) and off (AMS), showing the appearance of the $^{51}V^+$ peak due to the vaporization of soot particles.

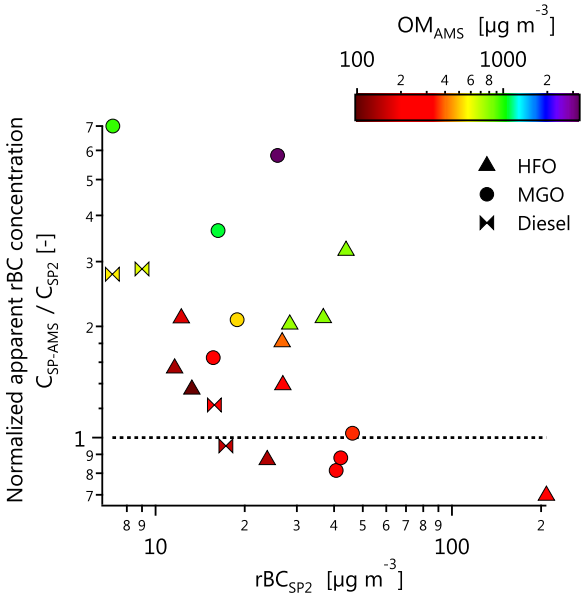

Figure S3: rBC concentrations as measured by SP-AMS ($C_{\mathrm{rBC,SP\text{-}AMS}}$) normalized by and plotted against rBC concentration measured by $C_{\mathrm{rBC,SP2}}$. Data for the two distillate fuels MGO and diesel are included for context (different symbols). Symbols are coloured by the AMS-measured OM concentration C_{OM}. While higher $C_{\mathrm{rBC,SP\text{-}AMS}} : C_{\mathrm{rBC,SP2}}$ was observed for higher C_{OM}, this must be interpreted with caution because C_{OM} variations were caused by changes in engine operating conditions. These changes also influenced particle number and median rBC-particle mass. In the concentration range 10–30 $\mu\mathrm{g\,m^{-3}}$, the required SP-AMS correction factor (i.e., E_z) spans a factor of 1–3.

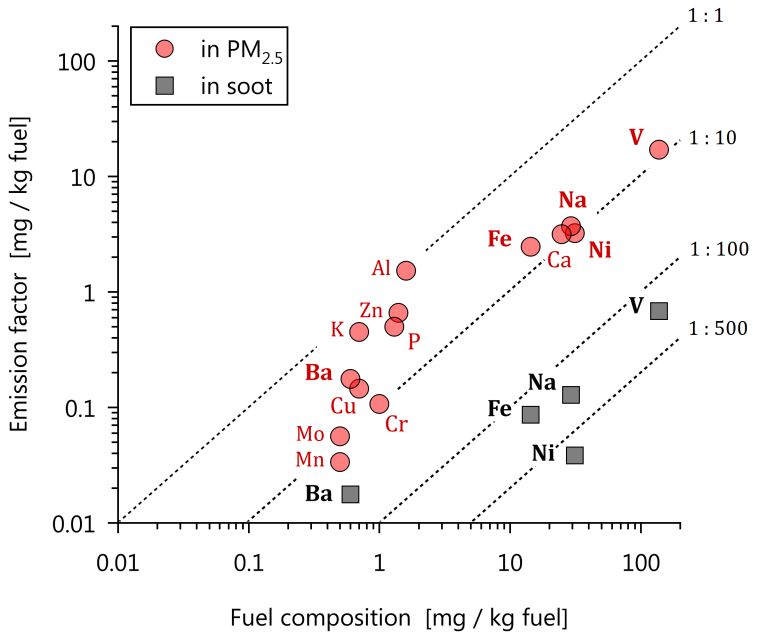

Figure S4: Elemental emission factors for in-$PM_{2.5}$ (ICP-OES) and in-soot (SP-AMS) measurements plotted against fuel composition. Symbols indicate the elements.

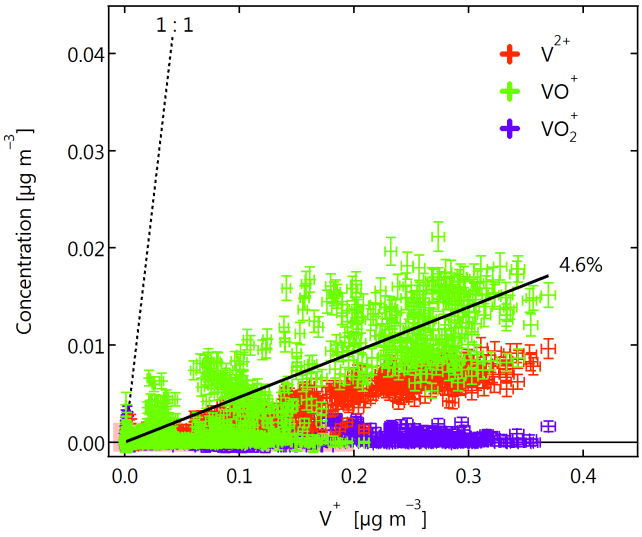

Figure S5: Vanadium-containing ions plotted against V^+. Black line: OLS fit excluding data below LOQ of $0.003\,\mu g\,m^{-3}$ VO^+ with intercept fixed at zero. Fit results given in Table S5. V^{2+} is included to demonstrate a lack of interference from nearby ions at V^+ (the intensity of $C_3H_7^{n+}$ relative to V^{n+} was much lower for the doubly-charged case). The units refer to the mass per volume of air in the sampled aerosol.

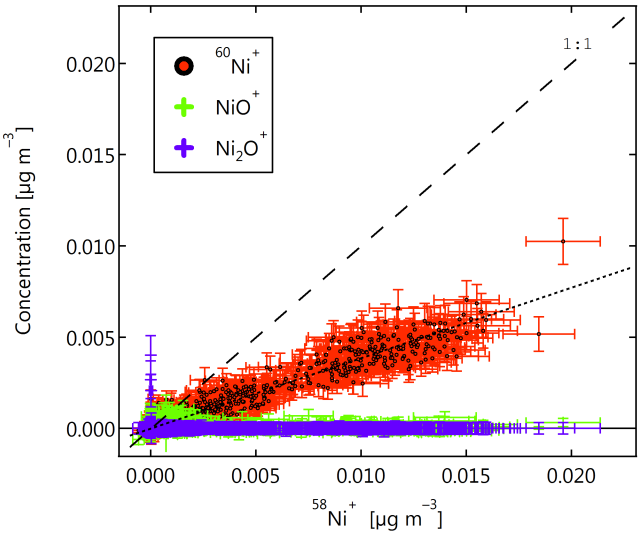

Figure S6: Nickel-containing ions and isotopes plotted against $^{58}Ni^+$. Dashed line shows 1 : 1; dotted line the expected relative abundance of 38.520%[15]. The units refer to the mass per volume of air in the sampled aerosol.

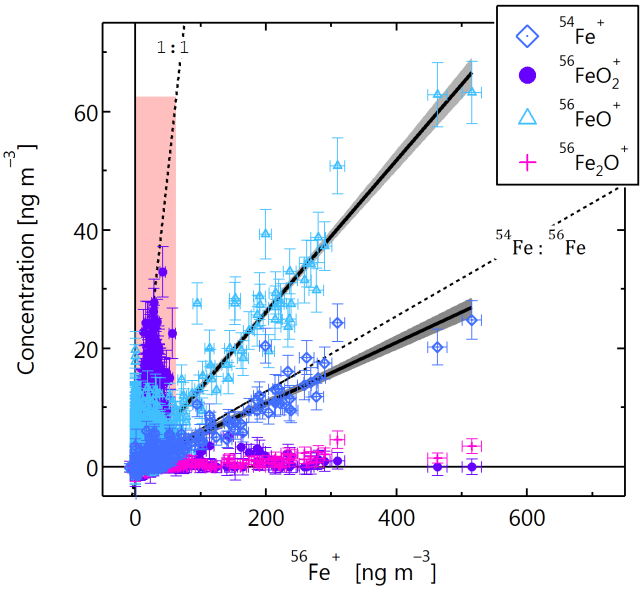

Figure S7: Iron-containing ions and isotopes plotted against the major iron isotope, $^{56}Fe^+$. Red shading shows the region in which FeO^+ was poorly correlated with $^{56}Fe^+$.Grey shading the 1 σ uncertainty of an OLS fit to data above LOQ. Lower dashed line shows the expected 6.3 % isotopic abundance of ^{54}Fe relative to ^{56}Fe[15].
The fits are ODR with intercepts were not significantly different from zero; fit slopes are given in Table S5. The units refer to the mass per volume of air in the sampled aerosol.

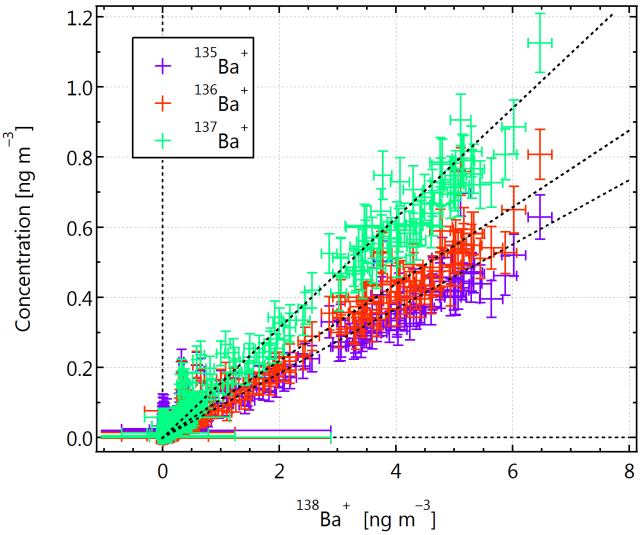

Figure S8: Isotopes of barium quantified by SP-AMS. Slopes are *not* fits to the data, but rather show the relative abundances of each isotope according to IUPAC[15]. The relative abundances are 9.194%, 10.954%, and 15.666% for Ba-135, Ba-136, and Ba-137, respectively. The units refer to the mass per volume of air in the sampled aerosol.

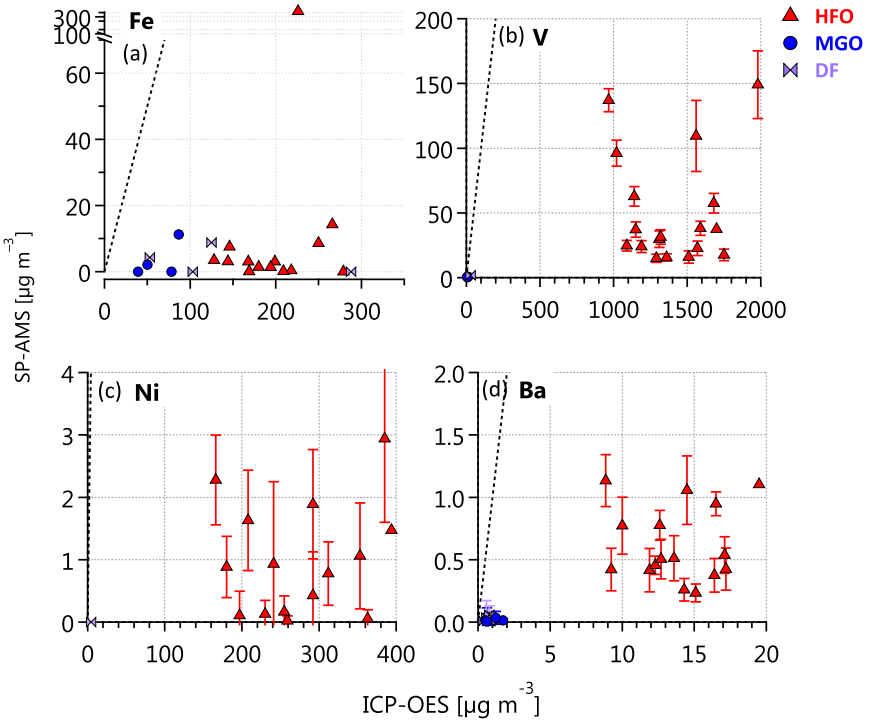

Figure S9: SP-AMS metal signals plotted against ICP-OES metal signals for (a-d) Fe, V, Ni and Ba, respectively. Note the split ordinate in panel (a).

References

(1) Canagaratna, M. et al. Chemical and microphysical characterization of ambient aerosols with the aerodyne aerosol mass spectrometer. *Mass Spectrom. Rev.* **2007**, *26*, 185–222.

(2) Eichler, P.; Müller, M.; Rohmann, C.; Stengel, B.; Orasche, J.; Zimmermann, R.; Wisthaler, A. Lubricating Oil as a Major Constituent of Ship Exhaust Particles. *Environ. Sci. Technol. Let.* **2017**, *4*, 54–58.

(3) Sippula, O.; Stengel, B.; Sklorz, M.; Streibel, T.; Rabe, R.; Orasche, J.; Lintelmann, J.; Michalke, B.; Abbaszade, G.; Radischat, C.; Grüger, T. M.; Schnelle-Kreis, J.; Harndorf, H.; Zimmermann, R. Particle Emissions from a Marine Engine: Chemical Composition and Aromatic Emission Profiles under Various Operating Conditions. *Environ. Sci. Technol.* **2014**, *48*, 11721–11729, PMID: 25202837.

(4) Streibel, T. et al. Aerosol emissions of a ship diesel engine operated with diesel fuel or heavy fuel oil. *Environmental Science and Pollution Research* **2017**, 10976.

(5) Matthew, B. M.; Middlebrook, A. M.; Onasch, T. B. Collection efficiencies in an Aerodyne Aerosol Mass Spectrometer as a function of particle phase for laboratory generated aerosols. *Aerosol Sci. Technol.* **2008**, *42*, 884–898.

(6) Aiken, A. C.; DeCarlo, P. F.; Jimenez, J. L. Elemental analysis of organic species with electron ionization high-resolution mass spectrometry. *Anal. Chem.* **2007**, *79*, 8350–8358.

(7) Aiken, A. C.; DeCarlo, P. F.; Kroll, J. H.; Worsnop, D. R.; Huffman, J. A.; Docherty, K. S.; Ulbrich, I. M.; Mohr, C.; Kimmel, J. R.; Sueper, D. O/C and OM/OC ratios of primary, secondary, and ambient organic aerosols with high-resolution time-of-flight aerosol mass spectrometry. *Environ. Sci. Technol.* **2008**, *42*, 4478–4485.

(8) Canagaratna, M.; Jimenez, J.; Kroll, J.; Chen, Q.; Kessler, S.; Massoli, P.; Hildebrandt Ruiz, L.; Fortner, E.; Williams, L.; Wilson, K.; Surratt, J.; Donahue, N.; Jayne, J.; DR, W. Elemental ratio measurements of organic compounds using aerosol mass spectrometry: characterization, improved calibration, and implications. *Atmos. Chem. Phys.* **2015**, *15*, 253–272.

(9) Onasch, T. B.; Trimborn, A.; Fortner, E. C.; Jayne, J. T.; Kok, G. L.; Williams, L. R.; Davidovits, P.; Worsnop, D. R. Soot Particle Aerosol Mass Spectrometer: Development, Validation, and Initial Application. *Aerosol Sci. Technol.* **2012**, *46*, 804–817.

(10) Carbone, S.; Onasch, T.; Saarikoski, S.; Timonen, H.; Saarnio, K.; Sueper, D.; Rönkkö, T.; Pirjola, L.; Häyrinen, A.; Worsnop, D.; Hillamo, R. Characterization of trace metals on soot aerosol particles with the SP-AMS: detection and quantification. *Atmos. Meas. Tech.* **2015**, *8*, 4803–4815.

(11) Svane, M.; Hagstrm, M.; Pettersson, J. B. C. Online Measurements of Individual Alkali-Containing Particles Formed in Biomass and Coal Combustion: Demonstration of an Instrument Based on Surface Ionization Technique. *Energy & Fuels* **2005**, *19*, 411–417.

(12) Heumann, K. G.; Eisenhut, S.; Gallus, S.; Hebeda, E. H.; Nusko, R.; Vengosh, A.; Walczyk, T. Recent developments in thermal ionization mass spectrometric techniques for isotope analysis. A review. *The Analyst* **1995**, *120*, 1291.

(13) Lyyränen, J.; Jokiniemi, J.; Kauppinen, E. I.; Joutsensaari, J. Aerosol characterisation in medium-speed diesel engines operating with heavy fuel oils. *J. Aerosol Sci.* **1999**, *30*, 771–784.

(14) Popovicheva, O.; Kireeva, E.; Shonija, N.; Zubareva, N.; Persiantseva, N.; Tishkova, V.; Demirdjian, B.; Moldanová, J.; Mogilnikov, V. Ship particulate pollutants: Characterization in terms of environmental implication. *J. Environ. Monit.* **2009**, *11*, 2077–2086.

(15) de Laeter, J. R.; Böhlke, J. K.; De Bièvre, P.; Hidaka, H.; Peiser, H.; Rosman, K.; Taylor, P. Atomic weights of the elements. Review 2000 (IUPAC Technical Report). *Pure Appl. Chem.* **2003**, *75*, 683–800.

(16) Corbin, J. C.; Othman, A.; Allan, J. D.; Worsnop, D. R.; Haskins, J. D.; Sierau, B.; Lohmann, U.; Mensah, A. A. Peak-fitting and integration imprecision in the Aerodyne aerosol mass spectrometer: effects of mass accuracy on location-constrained fits. *Atmos. Meas. Tech.* **2015**, *8*, 4615–4636.

(17) Liu, P. S. K.; Deng, R.; Smith, K. A.; Williams, L. R.; Jayne, J. T.; Canagaratna, M. R.; Moore, K.; Onasch, T. B.; Worsnop, D. R.; Deshler, T. Transmission Efficiency of an Aerodynamic Focusing Lens System: Comparison of Model Calculations and Laboratory Measurements for the Aerodyne Aerosol Mass Spectrometer. *Aerosol Sci. Technol.* **2007**, *41*, 721–733.

(18) Willis, M. D.; Lee, A. K. Y.; Onasch, T. B.; Fortner, E. C.; Williams, L. R.; Lambe, A. T.; Worsnop, D. R.; Abbatt, J. P. D. Collection efficiency of the Soot-Particle Aerosol Mass Spectrometer (SP-AMS) for internally mixed particulate black carbon. *Atmos. Meas. Tech.* **2014**, *7*, 4507–4516.

(19) Ahern, A. T.; Subramanian, R.; Saliba, G.; Lipsky, E. M.; Donahue, N. M.; Sullivan, R. C. Effect of secondary organic aerosol coating thickness on the real-time detection and characterization of biomass-burning soot by two particle mass spectrometers. *Atmos. Meas. Tech.* **2016**, *9*, 6117.

(20) Slowik, J. G.; Stainken, K.; Davidovits, P.; Williams, L.; Jayne, J.; Kolb, C.; Worsnop, D. R.; Rudich, Y.; DeCarlo, P. F.; Jimenez, J. L. Particle morphology and density characterization by combined mobility and aerodynamic diameter measurements. Part 2: Application to combustion-generated soot aerosols as a function of fuel equivalence ratio. *Aerosol Sci. Technol.* **2004**, *38*, 1206–1222.

(21) Kulkarni, G.; Pekour, M.; Afchine, A.; Murphy, D. M.; Cziczo, D. J. Comparison

of Experimental and Numerical Studies of the Performance Characteristics of a Pumped Counterflow Virtual Impactor. *Aerosol Sci. Technol.* **2011**, *45*, 382–392.

(22) Corbin, J. C.; Sierau, B.; Gysel, M.; Laborde, M.; Keller, A.; Kim, J.; Petzold, A.; Onasch, T. B.; Lohmann, U.; Mensah, A. A. Mass spectrometry of refractory black carbon particles from six sources: carbon-cluster and oxygenated ions. *Atmos. Chem. Phys.* **2014**, *14*, 2591–2603.

(23) Onasch, T. B.; Fortner, E. C.; Trimborn, A. M.; Lambe, A. T.; Tiwari, A. J.; Marr, L. C.; Corbin, J. C.; Mensah, A. A.; Williams, L. R.; Davidovits, P.; Worsnop, D. R. Investigations of SP-AMS Carbon Ion Distributions as a Function of Refractory Black Carbon Particle Types. *Aerosol Sci. Technol.* **2015**, *49*, 409–422.

(24) Corbin, J. C.; Keller, A.; Sierau, B.; Lohmann, U.; Mensah, A. A. Black-carbon-surface oxidation and organic composition of beech-wood soot aerosols. *Atmos. Chem. Phys.* **2015**, *15*, 11885–11907.

(25) Corbin, J. C.; Pieber, S. M.; Czech, H.; Zanatta, M.; Jakobi, G.; Massabò, D.; Orasche, J.; El Haddad, I.; Mensah, A. A.; Stengel, B.; Drinovec, L.; Močnik, G.; Zimmermann, R.; Prévôt, A. S. H.; Gysel, M. Brown and black carbon emitted by a marine engine operated on heavy fuel oil and distillate fuels: optical properties, size distributions, emission factors. *in prep.* **2017**,

(26) Chen, Y.; Shah, N.; Braun, A.; Huggins, F. E.; Huffman, G. P. Electron microscopy investigation of carbonaceous particulate matter generated by combustion of fossil fuels. *Energy & Fuels* **2005**, *19*, 1644–1651.

(27) Moteki, N.; Kondo, Y.; Takegawa, N.; Nakamura, S. Directional dependence of thermal emission from nonspherical carbon particles. *J. Aerosol Sci.* **2009**, *40*, 790–801.

(28) Slowik, J. G. et al. An Inter-Comparison of Instruments Measuring Black Carbon Content of Soot Particles. *Aerosol Sci. Technol.* **2007**, *41*, 295–314.

(29) Moteki, N.; Kondo, Y. Effects of Mixing State on Black Carbon Measurements by Laser-Induced Incandescence. *Aerosol Sci. Technol.* **2007**, *41*, 398–417.

(30) Park, K.; Kittelson, D. B.; Zachariah, M. R.; McMurry, P. H. Measurement of inherent material density of nanoparticle agglomerates. *J. Nanopart. Res.* **2004**, *6*, 267–272.

(31) Sorensen, C. The mobility of fractal aggregates: a review. *Aerosol Sci. Technol.* **2011**, *45*, 765–779.

(32) Cubison, M. J.; Jimenez, J. L. Statistical precision of the intensities retrieved from constrained fitting of overlapping peaks in high-resolution mass spectra. *Atmos. Meas. Tech.* **2015**, *8*, 2333–2345.

(33) Healy, R.; Hellebust, S.; Kourtchev, I.; Allanic, A.; O'Connor, I.; Bell, J.; Healy, D.; Sodeau, J.; Wenger, J. Source apportionment of PM 2.5 in Cork Harbour, Ireland using a combination of single particle mass spectrometry and quantitative semi-continuous measurements. *Atmos. Chem. Phys.* **2010**, *10*, 9593–9613.

(34) Ault, A. P.; Gaston, C. J.; Wang, Y.; Dominguez, G.; Thiemens, M. H.; Prather, K. A. Characterization of the Single Particle Mixing State of Individual Ship Plume Events Measured at the Port of Los Angeles. *Environ. Sci. Technol.* **2010**, *44*, 1954–1961.

(35) Liu, Z.; Lu, X.; Feng, J.; Fan, Q.; Zhang, Y.; Yang, X. Influence of Ship Emissions on Urban Air Quality: A Comprehensive Study Using Highly Time-Resolved Online Measurements and Numerical Simulation in Shanghai. *Environ. Sci. Technol.* **2017**, *51*, 202–211.

(36) Yau, P.; Lee, S.; Cheng, Y.; Huang, Y.; Lai, S.; Xu, X. Contribution of ship

emissions to the fine particulate in the community near an international port in Hong Kong. *Atmos. Res.* **2013**, *124*, 61–72.

(37) Quann, R.; Sarofim, A. Vaporization of refractory oxides during pulverized coal combustion. *Symp. (Int.) Combust.* **1982**, *19*, 1429–1440.